Informatics and Control Problems 46 Issue 1 (2026)
journal homepage: www.icp.az

Generalized synergistic edge-guided graph reasoning network for biomedical image segmentation

Di Zhao, Yi Tang*, Dmitry Pertsau, Alevtina Gourinovitch

Belarusian State University of Informatics and Radioelectronics, Minsk, Belarus

ARTICLE INFO

Article history:
Received 19.11.2025
Received in revised form 28.11.2025
Accepted 08.12.2025
Available online 20.03.2026

Keywords:
Medical image segmentation
Graph reasoning
Graph convolutional network
MRI
CT

ABSTRACT

Biomedical image segmentation plays a vital role in computer-aided diagnosis and treatment planning. However, existing methods often struggle with modeling complex anatomical structures and capturing long-range dependencies. To address these limitations, we propose a generalized Synergistic Edge-Guided Graph Reasoning Network (SEGRNet) that integrates convolutional feature extraction with graph-based global reasoning. The model projects pixel-level region and edge features into a graph domain, enabling adaptive interaction between local and global features via a graph convolutional network. After reasoning, enhanced features are mapped back for refined segmentation. Experiments conducted on three public datasets including BUSI, LGG and CHAOS outperforms state-of-the-art models in terms of dice coefficient, mean intersection over union and structural similarity. These results confirm the effectiveness and generalization ability of the proposed method across various medical imaging scenarios, making it suitable for future clinical applications.

1. Introduction

With the continuous advancement of medical imaging technologies, such as computed tomography (CT), magnetic resonance imaging (MRI), and positron emission tomography (PET), these imaging modalities have become indispensable tools for clinicians to assess and manage pathological conditions [1].

Despite the notable advancements in Convolutional Neural Networks (CNNs) based segmentation methods, they still exhibit several limitations. Primarily, CNNs are constrained by their finite receptive fields, which limits their ability to capture comprehensive global image information. Additionally, CNN models often require a large number of parameters and substantial computational resources, which can pose efficiency challenges in practical clinical settings. More critically, CNNs typically lack the ability to model the topological relationships between local features, which can diminish segmentation accuracy, especially when processing biological tissues with variable shapes and complex structures. To address these challenges, Graph Neural Networks (GNNs) have emerged as a novel and powerful solution. GNNs are adept at capturing the spatial relationships and interactions between pixel points by conducting convolutional operations over graph structures. Graph Convolutional Networks (GCNs) are a specific type of GNN that extends traditional convolutional operations from grid-like structures (e.g., images) to graph structures [2]. GCNs

*Corresponding author
E-mail addresses: carolzd0429@gmail.com (Di Zhao), tangyijcb@163.com (Yi Tang), pertsev@bsuir.by (Dmitry Pertsau), gurinovich@bsuir.by (Alevtina Gourinovitch)

www.icp.az/2026/1-05.pdf https://doi.org/10.54381/icp.2026.1.05

perform convolutions over graph nodes and their neighbors, enabling the aggregation of both local and global information, which allows them to better capture topological intricacies and retain global context compared to CNNs. This graph-based methodology enhances the model's capacity to integrate global information while preserving the spatial relationships of local features, which is critical for medical image segmentation where biological structures are often irregular and complex.

In this study we propose a generalized Synergistic Edge-Guided Graph Reasoning Network (SEGRNet), a medical image segmentation method that incorporates the strengths of CNNs in feature extraction with the advantages of GCNs in modeling graph structures. This hybrid approach enables a more holistic understanding of the image, leveraging CNNs for their efficient feature extraction capabilities and GCNs for their ability to model topological relationships within the data. To validate the effectiveness and generalizability of the proposed architecture, we conducted experiments on three diverse datasets across different imaging modalities (ultrasound, MRI, CT) and anatomical regions. This comprehensive evaluation reveals SEGRNet's robustness in handling inter-modality variations, tissue complexities, and boundary precision, providing a foundation for more sophisticated image analyses that better align with clinical demands.

2. Related work

Earlier studies, such as the U-Net architecture proposed by Ronneberger et al [3], successfully captured the contextual information in the image through a symmetric encoder-decoder structure and jump connections, laying the foundation for subsequent medical image segmentation tasks. However, U-Net is often difficult to ensure the accuracy of segmentation results when dealing with images with complex topology.

In order to solve this problem, Lu et al [4] tried to improve the accuracy of image segmentation by combining CNN with GNN and proposed the CNN-G model, which represents the image in the form of a graph and classifying the nodes by GNN. However, the method may have limitations when dealing with unstructured data. Meng et al. [5] enhanced segmentation performance by devising a graph-based deep learning framework that explicitly capitalizes on both regional and boundary features. Yet, this methodology may necessitate an increased volume of labeled data for training models, particularly when addressing the complexity and variability inherent in medical imaging. Then, Tepe et al [2] proposed an approach that combines hyperpixels and GNN to improve segmentation accuracy by converting images to graph structures and utilizing the powerful representational capabilities of GNN to capture long range dependencies in images. Nevertheless, the method still faces the challenge of computational resources when dealing with large-scale datasets. Jiang et al. [6] introduced the ViG-UNet, a GNN-based U-shaped architecture which outperforms most of the existing classical and state-of-the-art U-shape networks on multiple datasets. However, the approach may present challenges in terms of computational efficiency and parameter tuning in practical applications. In addition, Van De Vyver et al [7] proposed a GCN-based approach, which improves the robustness of segmentation by predicting the contour points of the heart structure rather than labeling each pixel. Although this method improves the accuracy of segmentation, it requires larger datasets for pre-training, which remains a challenge in the medical field.

To address these limitations, this article proposes a novel method that integrates CNN feature extraction with GCN-based global graph reasoning, overcoming challenges related to limited receptive fields and inadequate topological modeling in previous work. Additionally, by incorporating edge information into the reasoning process, the method enhances boundary detection and segmentation precision.

3. Architecture of the proposed network

As shown in Fig. 1, the proposed SEGRNet adopts Res2Net50 [8], pretrained on ImageNet, as its backbone. The input image is processed to extract multi-level feature maps, denoted as x_i ($i \in [1,2,\ldots,5]$). The first-level features have a unique spatial resolution $\frac{W}{2} \times \frac{H}{2}$, while a consistent resolution $\frac{W}{2^i} \times \frac{H}{2^i}$ is maintained for levels where i $>$ 1. The number of feature map channels at the ith layer is given as C_i (i = 1, 2, …, 5), and we have C = [64, 256, 512, 1024, 2048] according to [8]. What's more, as noted in [9], low-level features tend to capture fine-grained details such as edges and textures, whereas high-level features encapsulate more abstract semantic information crucial for object-level understanding and localization. Thus, in SEGRNet, low-level features from the first two layers are forwarded to a Contour-Guided Module (CGM), which is designed to enhance boundary detection by generating both an edge map and edge-aware features. Meanwhile, higher-level semantic features are processed by a Region-Guided Module (RGM) to extract meaningful contextual representations within object regions denoted as x_r.

Accurate edge modeling is essential in complex image segmentation tasks, where fine boundary delineation significantly affects overall performance. By explicitly incorporating edge information into the model, SEGRNet improves its sensitivity to boundary regions and enhances segmentation accuracy. Unlike conventional methods that simply concatenate edge and region features, SEGRNet employs a Synergistic Edge-Guided Graph Reasoning (SEGR) module, which uses GCNs to model the structured relationships between edge cues and semantic regions. In this formulation, both local and global interactions are captured by treating feature vectors as graph nodes, with edges representing dependencies and contextual relevance. Further, the fused features from the SEGR module are subsequently passed through a series of three 1×1 convolutional layers in the decoder, enabling progressive refinement and producing the final segmentation mask.

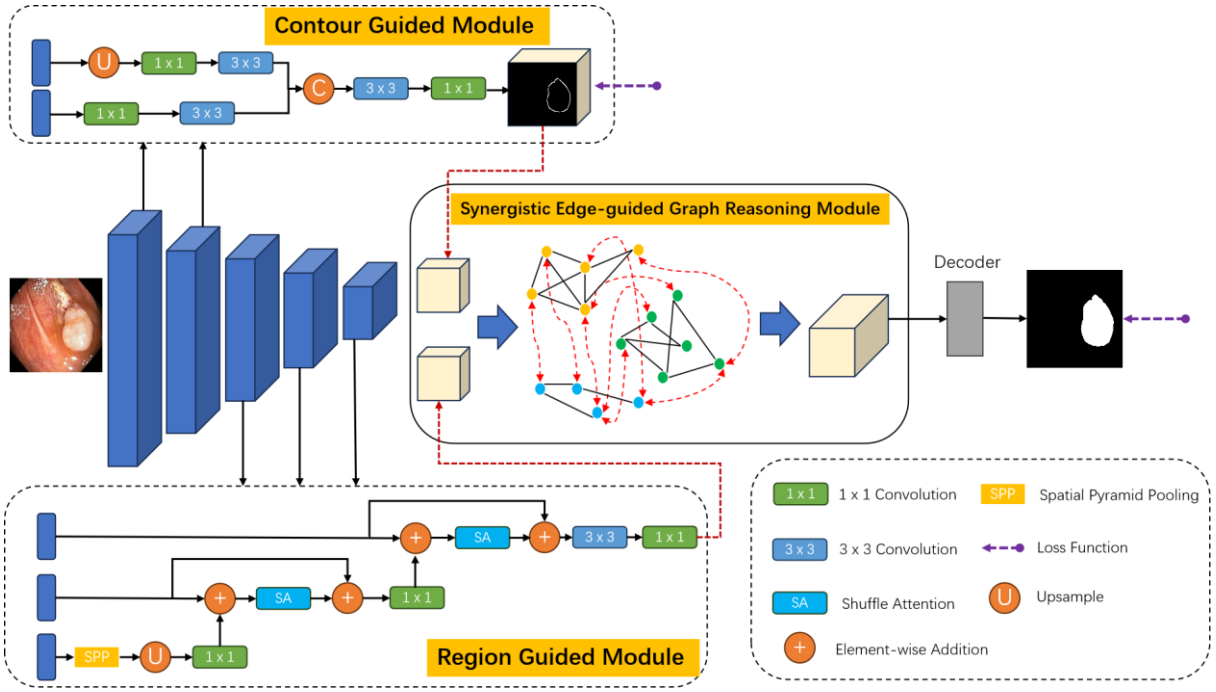

Fig. 1. Network architecture of the proposed synergistic edge-guided graph reasoning network

4. Synergistic Edge-guided Graph Reasoning Module

In modern convolutional neural networks, integrating spatial and contextual information is crucial for enhancing model performance, particularly in tasks requiring detailed spatial reasoning and feature interaction. To address these challenges, we propose the SEGR module, which effectively fuses edge and region-based semantic information, allowing the model to perform cohesive and adaptive reasoning across both feature sets.

The proposed SEGR module operates through three core steps: projection, interaction, and reverse projection. Fig.2 (a) shows the framework of graph reasoning idea. First, the region features are encoded into a global graph representation, where pixel clusters with similar features (regions) are projected onto vertices in an edge-aware manner. These vertices are then subjected to graph reasoning using a GCN layer, as opposed to conventional convolution operations, to explicitly model the relationships between different regions. In this interaction space, regions with similar semantics are represented by a single feature, simplifying the reasoning process across multiple regions. Simultaneously, edge information is also inserted and mapped to the interaction space, aggregating pixel features around the edges to emphasize boundary features, thus enabling more precise segmentation. After the reasoning process, the refined features are projected back onto the original pixel grid, yielding a feature map with enhanced detail.

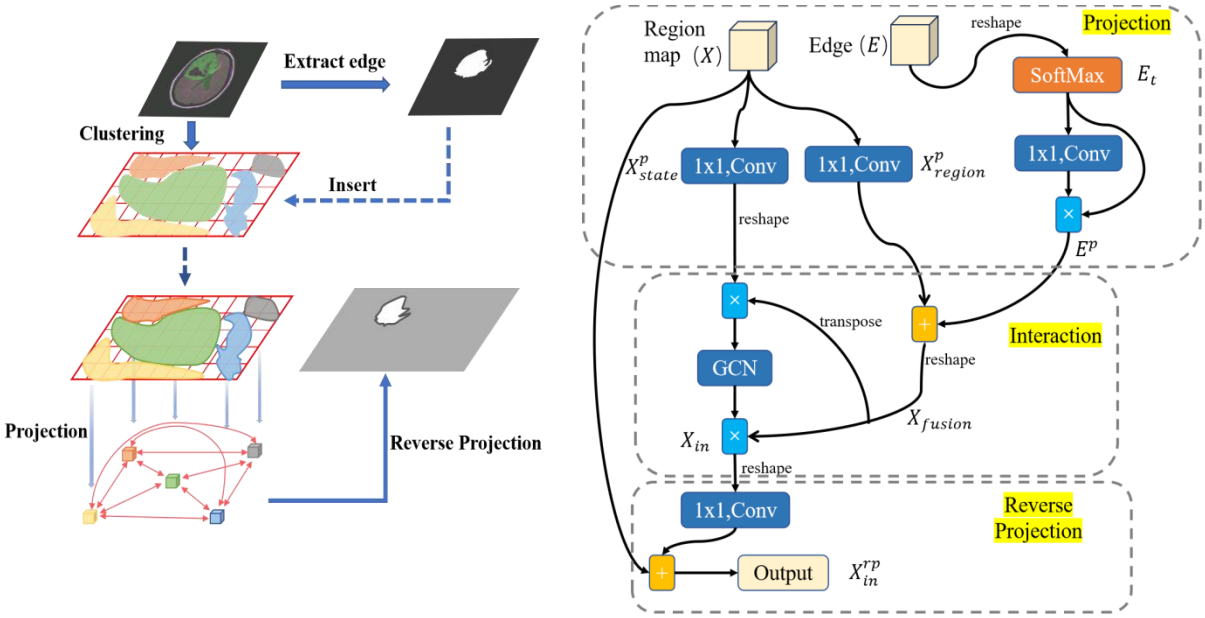

a) b)

Fig. 2. The schema of key idea:

a) the framework of graph reasoning; b) the structure of proposed SEGR module

Each step is designed to improve feature diversity and the model's global reasoning capability, particularly for complex scene understanding by leveraging both region and edge information. Below, each step is described in detail:

Projection. The input region map X is passed through two different 1×1 convolution operations, producing high-dimensional feature representations X^p_{state} and X^p_{region}. Meanwhile, the edge map E is resized to match the spatial dimensions of the input features. The resized edge features undergo a SoftMax operation, generating a normalized edge map E_t. Then it is passed through 1×1 convolution operation and element-wise multiplied with the normalized edge map to form weighted edge features denoted as E^p. This operation allows the model to better perceive structural boundaries, thus improving boundary recognition in complex scenes. The process can be formulated as follows:

$$X_{region}^{p} = \Psi_1(X) \tag{1}$$

$$X_{state}^{p} = \Psi_2(X) \tag{2}$$

$$E_t = \xi(resize(E)) \tag{3}$$

$$E^p = \Psi(E_t) \otimes E_t \tag{4}$$

where 'Ψ' denotes the 1×1 convolution with batch normalization and ReLU activation, 'ξ' and '$\otimes$' denote the SoftMax layer and element-wise multiplication respectively.

Interaction. This stage focuses on interaction between region and edge features using graph reasoning. The region features X_{region}^{p} and edge features E^p are first combined by element-wise addition, enhancing the representation of edge features. The fused features X_{fusion} are then reshaped as graph nodes, and global relationships are captured via matrix multiplication between the reshaped node features and the transposed fused features X_{fusion}^{T}. A GCN is applied to these node features for global reasoning, which models the relationships between distant regions. The output from the GCN is then combined with the original features through a residual connection, strengthening the contextual dependencies between different regions. This graph-based reasoning mechanism surpasses the limitations of conventional convolutions by capturing long-range semantic relationships, leading to more globally consistent feature representations in complex scenes. The process is represented as follows:

$$X_{fusion} = reshape(E^p + X_{region}^{p}) \tag{5}$$

$$X_{in} = GCN(X_{fusion}^{T} \otimes reshape(X_{state}^{p})) \otimes X_{fusion} \tag{6}$$

where X_{fusion}^{T} denotes the transpose of the fused features X_{fusion}, GCN denotes the graph convolution layer.

Reverse Projection. The graph-reasoned features are projected back onto the original feature space via matrix multiplication. This step reintegrates the global relationships learned during graph reasoning into the original pixel-level feature map. The result is then reshaped to match the dimensions of the original input, and a final 1×1 convolution is applied to restore the channel dimensions. A residual connection is used to combine these refined features with the original input, preserving local details while enhancing global feature expression through the interaction between regions and edges. This reverse projection enhances the model's ability to capture both fine-grained details and global structures, making it highly effective for tasks such as semantic segmentation. The reverse projection process is given as:

$$X_{in}^{rp} = \Psi(reshape(X_{in})) + X \tag{7}$$

5. Dataset Description

To train and validate the proposed model, we conducted experiments on three publicly available medical imaging datasets covering ultrasound, MRI, and CT modalities. The details of the datasets are as follows:

1. BUSI [10]: This dataset consists of breast ultrasound images collected from women aged 25 to 75. It includes a total of 780 images, categorized into 133 normal, 437 benign, and 210 malignant cases. Since normal images do not contain lesions, only the 647 benign and malignant images were used for training and evaluation.

2. LGG [11]: Provided by the National Cancer Institute's Cancer Imaging Archive, this dataset focuses on low-grade glioma (LGG) brain tumors. It includes FLAIR modality MRI scans from

TCGA patients, with abnormal regions manually annotated by neuroradiology experts to support supervised segmentation tasks.

3. CHAOS [12]: The Combined Healthy Abdominal Organ Segmentation (CHAOS) dataset comprises thousands of abdominal CT images with pixel-level annotations. In our study, we utilized 2,874 CT slices that include detailed liver segmentation labels.

For all three datasets, the images were randomly divided into training, validation, and test sets using an 8:1:1 ratio. A summary of the dataset statistics is provided in Table 1. Fields "Images", "Train", "Validation", "Test" denote the number of total images, training samples, validation samples and test samples respectively.

Table 1

Details of medical dataset used in the proposed experiments

Dataset	Images	Train	Validation	Test	Type	Application
BUSI	647	517	65	65	MRI	Breast
LGG	1310	1048	131	131	MRI	Gliomas
CHAOS	2874	2299	288	288	CT	Liver

6. Evaluation metrics

In this research, several standard evaluation metrics are employed to validate the effectiveness of our proposed method. Specifically, two commonly used metrics mean dice coefficient (mDice) and mean intersection over union (mIoU) were used. mDice is used to evaluate the similarity between model predictions and real labels in an image segmentation task. mIoU calculates the ratio between the intersection and concatenation between the predicted results and the true labels and averages it overall categories. Assuming that there is a total of N samples, and its calculation is shown below in Equation (8) and (9):

$$mDice = \frac{1}{N}\sum_{i=0}^{N}\frac{2 \cdot TP_i}{2 \cdot TP_i + FP_i + FN_i} \tag{8}$$

$$mIoU = \frac{1}{N}\sum_{i=0}^{N}\frac{TP_i}{TP_i + FP_i + FN_i} \tag{9}$$

where TP represents the number of true positives and FP represents the number of false positives. Additionally, according to [13] three widely used metrics in object detection are utilized including: S-measure (denoted as S_α), F-measure (denoted as F_ω), and E_Φ. S_α evaluates the structural similarity between region perception S_r and object perceptions S_o, while F_ω uses precision (denoted as P) and recall (denoted as R) to evaluate the performance of the model in an integrated manner. E_Φ captures both image-level statistics and local pixel matching, defined using an enhanced alignment matrix. These metrics provide a comprehensive evaluation of segmentation performance. The calculation is shown below in Equation (10)-(12):

$$S_\alpha = \alpha \times S_o + (1-\alpha) \times S_r \tag{10}$$

$$F_\omega = (1+\beta^2)\frac{P \times R}{\beta^2 P + R} \tag{11}$$

$$E_\Phi = \frac{1}{W \times H}\sum_{i=1}^{W}\sum_{i=1}^{H}\phi_{FM}(i,j) \tag{12}$$

where α is a trade-off parameter and it is set to 0.5 as default, β is set to 1 so that the accuracy and

completeness rates have the same weight, ϕ_{FM} denotes the enhanced-alignment matrix, 'W' and 'H' denote the width and height of images.

7. Training strategies and implementation details

To ensure a fair and consistent evaluation, we adopted a unified training strategy across all three medical image datasets. Considering the limited availability of labeled medical data, several data augmentation techniques were employed to improve generalization. These included random cropping, random rotation, horizontal and vertical flipping, and coarse dropout.

The model was implemented using PyTorch 1.13.1 and trained on a single NVIDIA 4060 Ti GPU with 16 GB of memory, using Python version 3.11. The Adam optimizer was employed due to its fast and stable convergence characteristics, with an initial learning rate set to 1e-4. All images were resized to 384×384 pixels during preprocessing. Training was conducted with a batch size of 16 for a maximum of 100 epochs.

To ensure result consistency, all baseline methods used for comparison were retrained and evaluated under the same experimental settings. It is important to note that no data augmentation was applied during the testing phase. Minor variations from original reported results may arise due to differences in the training environment and reimplementation conditions.

Table 2

Comparison of results on three datasets namely BUSI, LGG and CHAOS. The best results are in bold

Dataset	Method	mDice↑	mIoU↑	S_α ↑	F_ω ↑	E_Φ ↑
BUSI	Unet	0.576	0.584	0.726	0.417	0.759
	Unet++	0.708	0.628	0.789	0.589	0.748
	ResUnet++	0.687	0.631	0.729	0.608	0.782
	ACSNet	0.730	0.635	0.708	0.626	0.792
	DCRNet	0.748	0.666	0.719	0.686	0.803
	CFANet	0.759	0.689	0.774	**0.798**	0.826
	PraNet	0.787	0.711	0.753	0.768	**0.906**
	ours	**0.815**	**0.744**	**0.806**	0.793	0.849
LGG	Unet	0.806	0.734	0.879	0.829	0.909
	ResUnet	0.806	0.730	0.875	0.833	0.911
	ResUnet++	0.833	0.756	0.889	0.850	0.938
	CANet	0.829	0.750	0.888	0.849	0.930
	CFANet	0.800	0.714	0.871	0.827	0.922
	PraNet	0.817	0.731	0.883	0.854	0.938
	ours	**0.849**	**0.760**	**0.904**	**0.856**	**0.962**
CHAOS	FCN-8s	0.896	0.798	0.901	0.908	0.864
	ResUnet	0.903	0.787	0.910	0.915	0.900
	ResUnet++	0.922	0.810	0.924	0.931	0.926
	ICNet	0.931	0.843	0.938	0.946	0.920
	DANet	0.906	0.926	**0.983**	0.944	**0.972**
	PraNet	0.949	0.932	0.957	0.949	0.959
	ours	**0.970**	**0.954**	0.981	**0.961**	0.968

Results on BUSI Dataset. The BUSI dataset, known for its complexity in breast ultrasound image segmentation, presents significant challenges due to the subtle differences in tissue structures.

As presented in the Table 2, the proposed method achieved a remarkable performance, with a mDice of 0.815 and mIoU of 0.744, outperforming several baseline models. In particular, it exceeds U-Net by 41.1 percentage points in mDice (0.576) and U-Net++ by 10.7 points (0.708), highlighting its enhanced capacity to delineate fine structural boundaries. Compared to PraNet, a widely recognized model in the field, the proposed method achieved a 2.8% improvement in mDice. This indicates its superior ability to segment challenging cases where slight structural variations in breast tissues are crucial, leading to more precise diagnostic outcomes. The model's resilience in capturing finer details offers a significant advantage in clinical applications, where accuracy is paramount.

Results on LGG Dataset. The LGG dataset is a widely recognized benchmark in the field of brain tumor segmentation, providing highly detailed and complex data that challenges the segmentation capabilities of various models. The proposed model demonstrated superior performance across all evaluated metrics, with a mDice of 0.849, mIoU of 0.760, S_α of 0.904, F_ω of 0.856, and E_Φ of 0.962. In comparison, ResUnet++ achieved a mDice of 0.833 and mIoU of 0.756, highlighting the proposed model's clear improvements, particularly in mIoU, which is critical for assessing the overlap between predictions and ground truth labels. Moreover, the proposed model surpassed PraNet, which had a mDice of 0.817 and mIoU of 0.731, emphasizing its ability to enhance segmentation precision and recall, both essential in clinical brain tumor detection tasks. Additionally, the higher S_α (0.904) and E_Φ (0.962) values indicate that the model performs well in maintaining structural integrity and capturing image-level statistics, further demonstrating its robustness in handling complex brain tumor structures. These improvements are crucial for providing reliable results in real-world clinical settings, where accurate and detailed segmentation is required for treatment planning.

Results on CHAOS Dataset. The CHAOS dataset, focused on multi-organ segmentation, presents unique challenges due to the varying sizes and shapes of abdominal organs. The proposed model delivered outstanding results, achieving a mDice of 0.970, mIoU of 0.954, S_α of 0.981, F_ω of 0.961, and E_Φ of 0.968, outperforming all other models. For instance, compared to ICNet, which obtained a mDice of 0.931 and mIoU of 0.843, the proposed model demonstrated significant improvements, especially in mIoU and S_α, which assess the spatial overlap and structural similarity, respectively. Additionally, compared to PraNet, which achieved a mDice of 0.949 and mIoU of 0.932, the proposed model exhibited superior precision, particularly in F_ω(0.961), which reflects the model's balanced performance across all regions and boundaries. The higher E_Φ(0.968) further underscores the model's ability to align predictions with ground truth at both local and global scales. These improvements are critical in segmenting complex organ boundaries, such as the liver and kidneys, ensuring more accurate and reliable results. This robust performance demonstrates the model's suitability for clinical applications, where accurate segmentation is essential for diagnosis, treatment planning, and surgical interventions.

8. Qualitative results and visualization

In the in-depth analysis of model performance, Fig.3 visually presents the comparison between the predicted masks and the ground truth masks across three different datasets. The results demonstrate that the model achieves accurate segmentation even in scenarios with numerous and small-sized targets. Additionally, for regions with complex and irregular boundaries, the model also exhibits high segmentation accuracy. This indicates that the model possesses excellent generalization ability and a strong capacity for capturing details, particularly when handling challenging image segmentation tasks.

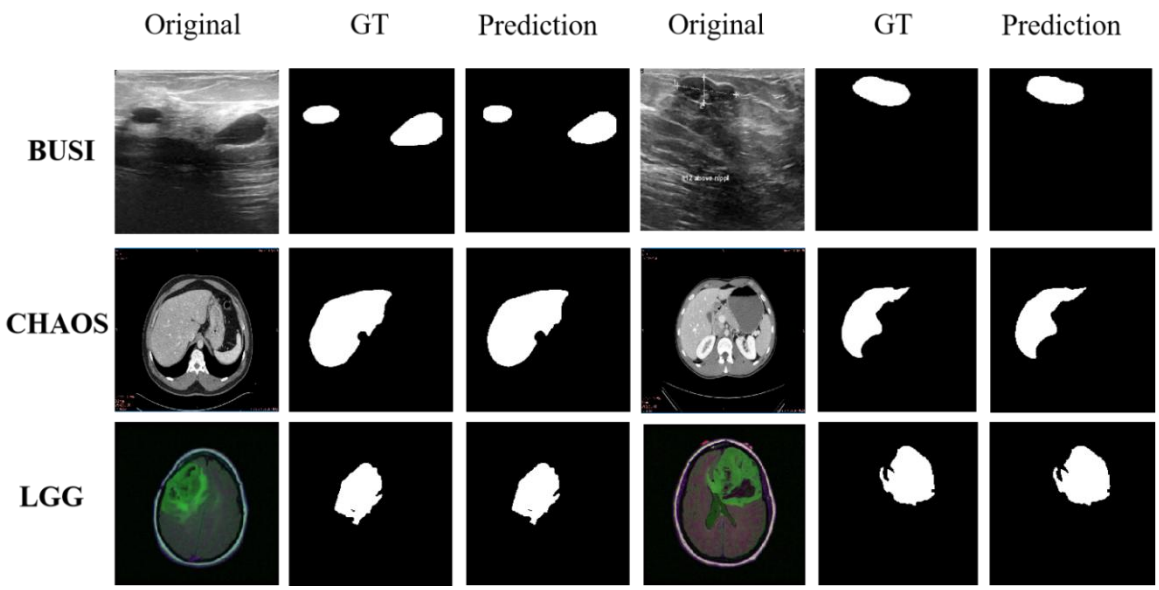

Fig.3. Visualization and training loss variations

To further evaluate the model's complexity and inference efficiency, Fig.4(a) shows the Average Precision-Recall (APR) curve across three datasets, which provides a balanced assessment of the trade-off between precision and recall. When compared to other state-of-the-art segmentation methods, proposed model outperforms others on the PR curve, suggesting that it not only accurately identifies lesion regions but also effectively reduces the occurrence of missed detections. This performance improvement demonstrates the superiority of the model in medical image segmentation tasks and its potential for practical clinical applications, offering more reliable and accurate diagnostic support, which is critical for improving diagnostic accuracy and reducing medical errors. Furthermore, the superior performance on the APR curve across the three datasets highlights the robustness and generalization capability of the proposed method. Fig.4(b) shows that on BUSI, LGG, and CHAOS the training loss decreases smoothly and almost monotonically, indicating stable learning without oscillations. Most of the reduction happens by around 90 epochs, after which the curves flatten, demonstrating that the model reaches near-convergence by 100 epochs. This rapid and consistent convergence across all datasets underscores the model's ability to capture diverse imaging features efficiently.

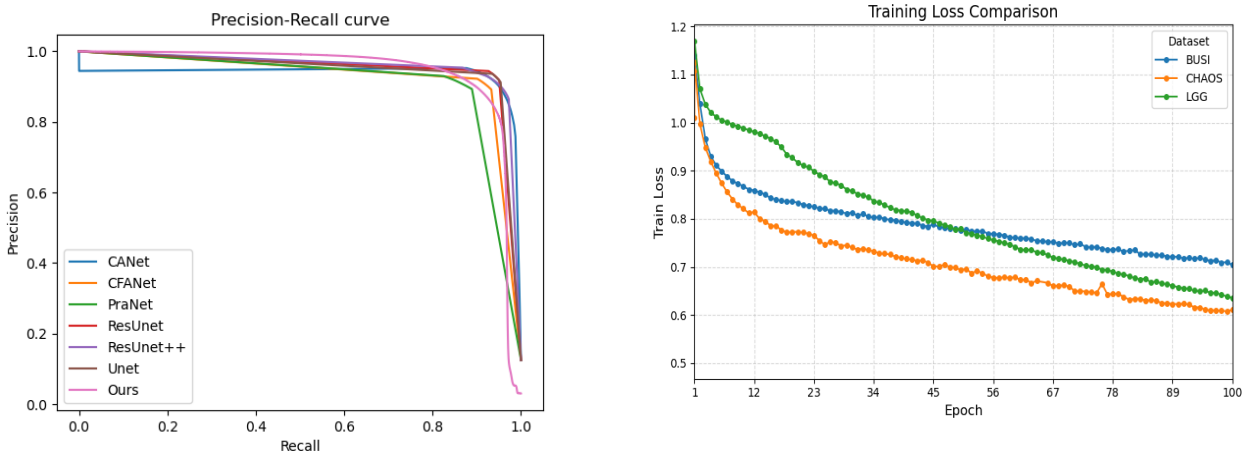

a) b)

Fig.4. Visualization of model performance on three datasets:
a) the average precision-recall curves; b) training loss over 100 epochs

Lastly, to investigate model complexity and inference time, Fig.5 reports the model sizes and computational complexity compared to other methods. Parameters are measured in millions (M), and floating-point operations (FLOPs) are measured in billions (G). As shown, our model utilizes the second fewest parameters, indicating its lightweight design. Additionally, the moderate computational complexity suggests that the model can capture complex data patterns while maintaining low computational costs.

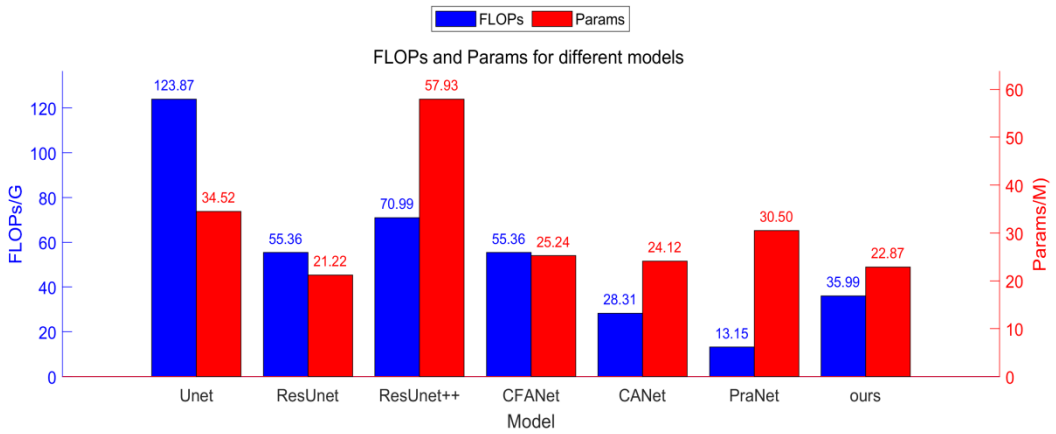

Fig.5. Comparison of model parameters and FLOPs

9. Conclusion

This study aims to enhance the accuracy and stability of biomedical image segmentation algorithms in complex medical images without compromising computational efficiency. Therefore, a novel Edge-Guided Graph Reasoning Network (SEGRNet) was proposed for biomedical image segmentation, which combines the feature extraction capabilities of CNNs with the powerful global reasoning abilities of GCNs. This network initially utilizes CNNs to encode regional features from medical images into a global graph representation, while simultaneously mapping edge information onto the graph to emphasize edge pixels during the feature aggregation process. Graph reasoning through GCNs allows for global interaction between regions, and after the reasoning is completed, the refined features are projected back onto the original pixel grid, generating a feature map enriched with detail.

To evaluate the segmentation efficiency and generalization capability of the model, the proposed SEGRNet was evaluated on three different datasets: BUSI, LGG, and CHAOS with several evaluation metrics such as mDice and mIoU. The experimental results demonstrate that the method provides a promising avenue for advancing medical image segmentation by addressing challenges associated with traditional CNN-based approaches, including limited receptive fields and deficiencies in topological modeling. The experimental results across three datasets not only demonstrate the model's segmentation accuracy but also underline its domain adaptability and practical scalability. Future work will further explore its deployment in real-time systems and collaboration with domain experts for clinical validation across more challenging and rare datasets.

References

[1] G. Litjens, T. Kooi, B.E. Bejnordi, A.A.A. Setio, F. Ciompi, M. Ghafoorian, J. A.W.M. van der Laak, B. van Ginneken, C.I. Sánchez, A survey on deep learning in medical image analysis, Medical Image Analysis. 42 (2017) pp.60-88. https://doi.org/10.1016/j.media.2017.07.005

[2] E. Tepe, G. Bilgin, Graph neural networks for colorectal histopathological image classification, IEEE Medical Technologies Congress. (2022) pp.1-4. https://doi.org/10.1109/TIPTEKNO56568.2022.9960184

[3] O. Ronneberger, P. Fischer, T. Brox, U-net: Convolutional networks for biomedical image segmentation, Medical Image Computing and Computer-Assisted Intervention, MICCAI 2015. (2015) pp.234-241. https://doi.org/10.1007/978-3-319-24574-4_28

[4] Y. Lu, Y. Chen, D. Zhao, B. Liu, Z. Lai, J. Chen, CNN-G: Convolutional neural network combined with graph for image segmentation with theoretical analysis, IEEE Transactions on Cognitive and Developmental Systems. 13 No.3 (2020) pp.631-644. https://doi.org/10.1109/TCDS.2020.2998497

[5] Y. Meng, H. Zhang, Y. Zhao, X. Yang, Y. Qiao, I.J.C. MacCormick, Graph-based region and boundary aggregation for biomedical image segmentation, IEEE Transactions on Medical Imaging. 41 No.3 (2021) pp.690-701. https://doi.org/10.1109/TMI.2021.3123567

[6] J. Jiang, X. Chen, G. Tian, Y. Liu, ViG-UNet: vision graph neural networks for medical image segmentation, IEEE 20th International Symposium on Biomedical Imaging. (2023) pp.1-5. https://doi.org/10.1109/ISBI53787.2023.10230496

[7] G. Van De Vyver, S. Thomas; G. Ben-Yosef, S.H. Olaisen, H. Dalen, L. Løvstakken, Towards Robust Cardiac Segmentation using Graph Convolutional Networks, IEEE Access. 12 (2024) pp.33876-33888. https://doi.org/10.1109/ACCESS.2024.3373046

[8] S.-H. Gao, M.-M. Cheng, K. Zhao, X.-Y. Zhang, M.-H. Yang, P. Torr, Res2Net: A New Multi-Scale Backbone Architecture, IEEE Transactions on Pattern Analysis and Machine Intelligence. 43 No.2 (2021) pp.652-662. https://doi.org/10.1109/TPAMI.2019.2938758

[9] Z. Zhang, H. Fu, H. Dai, J. Shen, Y. Pang, L. Shao, ET-net: A generic edge-attention guidance network for medical image segmentation, Medical Image Computing and Computer Assisted Intervention – MICCAI 2019. pp.442-450. https://doi.org/10.1007/978-3-030-32239-7_49

[10] W. Al-Dhabyani, M. Gomaa, H. Khaled, A. Fahmy, Dataset of breast ultrasound images, Data in brief, 28 (2020) 104863. https://doi.org/10.1016/j.dib.2019.104863

[11] M. Buda, A. Saha, M. A. Mazurowski, Association of genomic subtypes of lower-grade gliomas with shape features automatically extracted by a deep learning algorithm, Computers in Biology and Medicine. 109 (2019) pp.218-225. https://doi.org/10.1016/j.compbiomed.2019.05.002

[12] A.E. Kavur, N.S. Gezer, M. Barış, S. Aslan, P.-H. Conze, V. Groza, D.D. Pham, S. Chatterjee, P. Ernst, S. Özkan, B. Baydar, D. Lachinov, S. Han, J. Paul, F Isensee, M. Perkonigg, R. Sathish, R. Rajan, D. Sheet, G. Dovletov, A. Selver, CHAOS challenge-combined (CT-MR) healthy abdominal organ segmentation, Medical Image Analysis. 69 (2021) 101950. https://doi.org/10.1016/j.media.2020.101950

[13] T. Zhou, Y. Zhou, K. He, C. Gong, J. Yang, H. Fu, D. Shen, Cross-level feature aggregation network for polyp segmentation, Pattern Recognition. 140 (2023) 109555. https://doi.org/10.1016/j.patcog.2023.109555